Q. J. R. Meteorol. Soc. (1996), **122**, pp. 1597–1623

Dynamics of cumulus rising into stratocumulus as observed during the first 'Lagrangian' experiment of ASTEX

By STEPHAN R. de ROODE* and PETER G. DUYNKERKE
University of Utrecht, The Netherlands

(Received 7 March 1995; revised 22 December 1995)

SUMMARY

The Atlantic Stratocumulus Transition Experiment took place during June 1992 in the eastern Atlantic Ocean in an area extending south-east of the Azores to Madeira. One of the goals of this experiment was to study the physical processes responsible for the transition from stratocumulus to shallow cumulus clouds. The cloud type most frequently observed was cumulus rising into stratocumulus. Two 'Lagrangian' experiments were carried out to study the evolution of the boundary layer and to observe any transition in the cloud characteristics downstream.

Here we concentrate on the last flight of the first 'Lagrangian' experiment during which cumulus cloud was penetrating thin and broken stratocumulus from below. The immediate cause of the cumulus convection was condensation at the top of the well-mixed surface-based boundary layer. The lifting condensation level was observed to be at about 500 m and above this height there was a conditionally unstable layer up to 1600 m. In the upper part of the conditionally unstable layer the horizontally averaged thermodynamical variables showed that the air was very close to saturation, indicating that the upper part of the cloud deck consisted of broken clouds. The vertical structure of mean variables, variances, fluxes and turbulent kinetic energy budget is discussed. One of the findings is that the cumulus convection is an important factor in counteracting the gradual dissipation of the stratocumulus deck in that it supplies moisture to the latter. Furthermore, the net longwave radiative loss at cloud top was observed to be about 40 ± 15 W m^{-2}, which tended to destabilize the cloud layer from above. The skewness factor S showed that the upward convection was quite intense owing to the rising cumuli, the factor S reaching a maximum of about 2 ± 0.7 in the middle of the cloud layer. The skewness was found to be slightly negative near the cloud top.

KEYWORDS: Cloud dynamics Cloud radiative properties Cumulus penetration Marine stratocumulus

1. INTRODUCTION

Extensive areas of cumulus and stratocumulus clouds cover most of the tropical oceans. In the subtropics stratocumulus is found primarily below a strong capping inversion caused by subsidence in the Hadley circulation cell. As the boundary-layer air moves equatorwards over sea with an increasing surface temperature, the stratocumulus gradually breaks up into cumulus (Klein and Hartmann 1993). Some of the physical processes that influence this transition are subsidence, drizzle, entrainment (Caughey *et al.* 1982; Deardorff 1976; Weaver and Pearson 1990) and decoupling of the boundary layer (Turton and Nicholls 1987; Nicholls and Leighton 1986; Hignett 1991).

The turbulence structure of stratocumulus has been thoroughly studied recently by way of measurements made by Brost *et al.* (1982a, 1982b), Caughey *et al.* (1982), Caughey and Kitchen (1984), Roach *et al.* (1982), Slingo *et al.* (1982a, 1982b), Albrecht *et al.* (1985), Rogers and Telford (1986), Nicholls and Leighton (1986), Nicholls (1984, 1989), Hignett (1991) and Paluch and Lenschow (1991); see review by Driedonks and Duynkerke (1989). Typically it is found that cloud-top cooling is the dominant buoyancy production term and the main mechanism producing turbulent kinetic energy (TKE). Consequently the buoyancy flux and TKE are found to be at a maximum in the upper part of the cloud layer. Nicholls (1989) has shown that just below the stratocumulus cloud top the primary convective elements are, typically, negatively buoyant downdraughts. All these observational studies have greatly increased our understanding of stratocumulus dynamics.

In boundary layers containing cumulus clouds the production of TKE is triggered off by instability at the surface which gives rise to convective thermals. If the lifting

---

* Corresponding author: Institute for Marine and Atmospheric Research Utrecht (IMAU), Utrecht University, Princetonplein 5, 3584 CC Utrecht, The Netherlands.

condensation level is in a conditionally unstable layer, and if the cloud has enough vertical momentum and there is a sufficient release of latent heat then the cloud can reach its level of free convection, at which level it obtains a positive buoyancy again (Stull 1985). The thermal induces its own pressure perturbation, which affects its evolution and draws more air in through its cloud base. The lifetime of this cumulus cloud is controlled by its own dynamics and interaction with the environment. Initially most observational studies on cumulus were based on large-scale budget results obtained from field experiments such as BOMEX (Barbados Oceanographic and Meteorological Experiment) (Holland and Rasmusson 1973) and ATEX (Atlantic Tradewind Experiment) (Augstein *et al.* 1973). In the 70s and 80s detailed observational studies of the turbulence structure of cumulus were made during the Puerto Rico Field Experiment (Pennell and LeMone 1974; LeMone and Pennell 1976), the GARP (Global Atmospheric Research Program) Atlantic Tropical Experiment (GATE), (Nicholls and LeMone 1980) and the Boundary-Layer Experiment-1983 (Stull and Elorante 1984). Recently the dynamics of fields of cumulus over the sea around the British Isles have also been described (Smith and Jonas 1995). However, although there have been numerous observational studies of stratocumulus dynamics, very few detailed observational cases of cumulus dynamics are available. Most of the observations of the cumulus concentrated on the dynamics in the subcloud layer only.

The radiative and dynamical properties of stratocumulus and cumulus clouds are very different. Therefore it is important to understand the conditions under which stratocumulus and cumulus are formed and maintained. An ideal experiment is, therefore, to study the transition from stratocumulus to cumulus clouds in the Hadley circulation. This transition we are currently investigating using data from ASTEX (Atlantic Stratocumulus Transition Experiment). More specifically, we are analysing aircraft data from the first 'Lagrangian' experiment of ASTEX (Fig. 1). Duynkerke *et al.* (1995) analysed the detailed microphysical and turbulence structure of the stratocumulus observed on flight A209. For a description of the evolution of the boundary layer during the first 'Lagrangian' experiment refer to Bretherton and Pincus (1995) and Bretherton *et al.* (1995). In these papers the mean vertical structure of the boundary layer, cloudiness and entrainment are discussed. The aim of this paper is to present the results of flight A210, during which cumulus was penetrating, from below, into a thin and broken stratocumulus layer. We shall focus on the mean structure, turbulence and radiative characteristics of the boundary layer. Since both types of cloud were observed, the results should help us to gain a better understanding of the dynamics of the transition from stratocumulus to cumulus clouds.

2. INSTRUMENTATION, FLIGHT PLAN AND SYNOPTIC SITUATION

(*a*) *ASTEX*

The ASTEX observational programme was carried out in the period 1–28 June 1992 from bases on the islands of Santa Maria and Porto Santo (Fig. 1), and involved aircraft, buoys, satellite platforms and land-based and ship-based observations. Here we shall focus on the last flight of the first 'Lagrangian' experiment which was made with the C-130 aircraft belonging to the UK Meteorological Research Flight (MRF). The aircraft base during ASTEX was on the island of Santa Maria, where surface-based measurements were made. For the purpose of collecting spatial information for the entire period of the experiment the German ship *Valdivia* was located at about position 27 °N, 24 °W; also, surface-based measurements were made on the island of Porto Santo. In addition satellite and radiosonde data were collected for this observational area. Some of the advantages of these locations are that they are often little affected by anthropogenically polluted air from

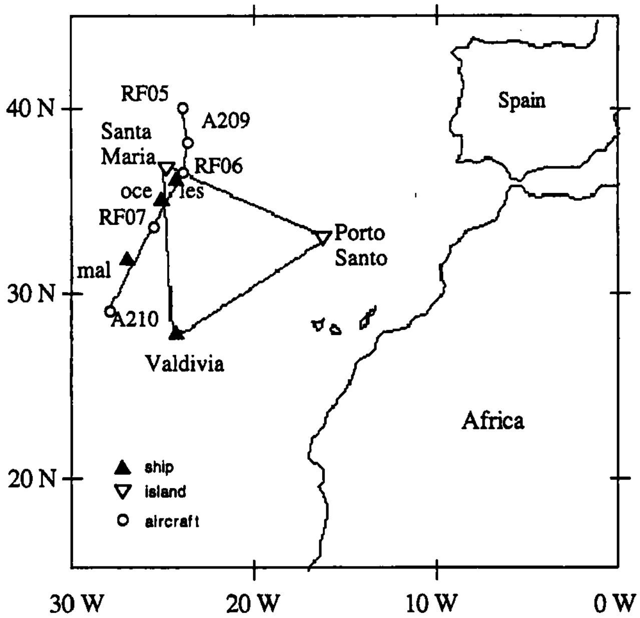

Figure 1. Map of ASTEX region showing the observation triangle. The curved line shows the trajectory of the first Lagrangian (from north to south) from 1600 UTC 12 June until 1600 UTC 14 June 1992. Indicated are the ASTEX triangle and the flights (open circles) of the NCAR Electra (RF05, RF06 and RF07) and the UK MRF C-130 (A209 and A210). Also shown are the locations of the radiosonde stations at 1200 UTC 14 June 1992: the islands (open triangles) of Porto Santo and Santa Maria, the ships (filled triangle) *Valdivia*, *Malcolm Baldridge* (mal), *Oceanus* (oce) and *Le Suroit* (les).

the continent; the synoptic situation in this region is quite stationary and both stratocumulus and cumulus clouds are present.

The first 'Lagrangian' experiment lasted from 1600 UTC on 12 June until 1600 UTC on 14 June 1992. Within this period the boundary layer deepened, wind speeds were moderate to high and there was substantial drizzle. A solid well-mixed stratocumulus-topped boundary layer 700 m thick developed into a layer filled mainly with cumulus penetrating into thin and broken stratocumulus above, as observed during flight A210.

(*b*) *Instrumentation*

The primary instrumentation on board was specially adapted for observations of turbulence, radiation and cloud physics. Table 1 lists the main instruments used in this study. More detailed information can be found in the ASTEX operational plan (1992). The total specific humidity, q_T, was measured directly (Table 1), and can also be calculated from the independent measurements of specific humidity, q_v, and liquid water content, q_l, made with the Johnson–Williams (J–W) meter. The ratio $r = q_T/(q_v + q_l)$ was calculated as a check on the measurement accuracy. We found that r deviated from unity by about 2% in the cloud and subcloud layer. We calculated q_l from the Forward Scattering Spectrometer Probe (FSSP), compared the result with the J–W meter measurements and found differences as large as 50%. During flight A209, when a solid stratocumulus layer was present, the discrepancy between the measurements made by the two instruments was found to be much smaller (Duynkerke *et al.* 1995). A possible explanation of these differences during flight A210 could be any one of a high liquid water content, large droplet sizes in the cumuli, which can lead to an underestimation of the liquid water content by the FSSP, or a broken cloud structure and an insufficient time response of the J–W meter (Gerber *et*

TABLE 1. SUMMARY OF MAIN INSTRUMENTS USED IN THIS STUDY AND ON BOARD THE C-130 (FROM THE ASTEX OPERATIONS PLAN).

Parameter	Device	f (Hz)	Accuracy
Static pressure	Rosemount 1201F	32	±1 hPa
Horizontal wind component	Pitot-static system, inertial navigation system (G.P.S.), angle of side slip vane	32	±0.4 m s^{-1}
Vertical wind speed	Pitot-static system, angle of attack vane	32	±0.1 m s^{-1}
Temperature	Rosemount 102BL platinum resistance thermometer	32	±0.03 °C
Dew point temperature	Thermoelectric hygrometer	4	±0.5 °C (>0 °C) ±1.0 °C (<0 °C)
Altitude	Radar altimeter	1	±1 m
Total water	Lyman-alpha absorption hygrometer	64	±0.15 g kg^{-1}
Liquid water	Johnson–Williams meter	4	±10%
Infrared radiation	Pyrgeometer (developed by UK Met Office)	1	±3%
Visible radiation	Pyranometer	1	±1%
Radiometric surface temperature	Barnes PRT 4 (modified by MRF)	1	±0.6 °C
Cloud droplet spectrum	Laser spectrometer, FSSP	1	

al. 1994). To calculate the liquid water flux, $\overline{w'q_l'}$, we used the J–W meter data since its measurement frequency is four times higher than that of the FSSP.

Determining the vapour flux accurately from dew point and pressure was problematical for the lowest and highest runs within the boundary layer. At these heights, much of the turbulence is contained in the small-scale eddies. From the spectra of the specific humidity it was found that only those of total specific humidity showed an inertial subrange. Therefore, the measurements of the total specific humidity were used for determining the vapour flux, calculated as the difference between the total and liquid-water flux in the cloud layer.

To calculate vertical fluxes we used filtered data. The filter used is described by Nicholls (1989). We calculated a 31-seconds running-mean and subtracted it from the raw data, whereupon we applied the eddy correlation technique. This enabled us to filter out variations larger than about 3 km, thus neglecting the low-wavenumber contribution to the flux. Analysis of the vertical-velocity spectra showed that the spectral peak was located within this range.

(*c*) *Flight plan*

Figure 2 shows the aircraft height as a function of time for flight A210. Three different flight methods were used: horizontal runs, profile flights and one porpoise run. One horizontal run (indicated by the capital letter R in Fig. 2) lasted typically for about 10 minutes. Since the average aircraft speed was about 100 m s^{-1} the run covered a horizontal distance of approximately 60 km. Because on Run 1 a set of eight horizontal runs were flown, the vertical resolution is quite coarse and details like the temperature jump in the inversion layer are not resolved. To supplement our information we also used data from profile flights (P in Fig. 2). The profile soundings were made along a flight path with a 2° inclination.

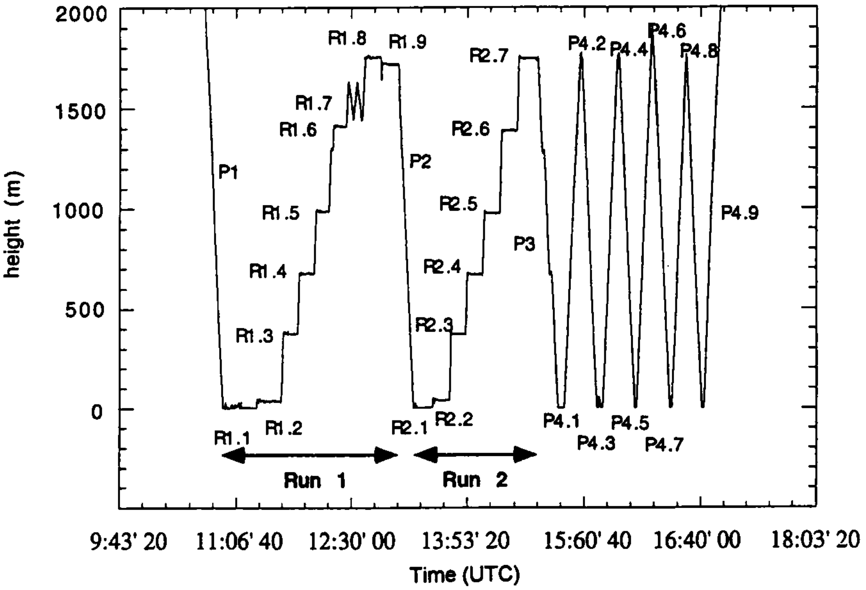

Figure 2. Aircraft height during flight A210 as a function of time in UTC. Profile flights are abbreviated to 'P', the horizontal runs to 'R'. Flight R1.7 is a porpoising run above and through cloud tops.

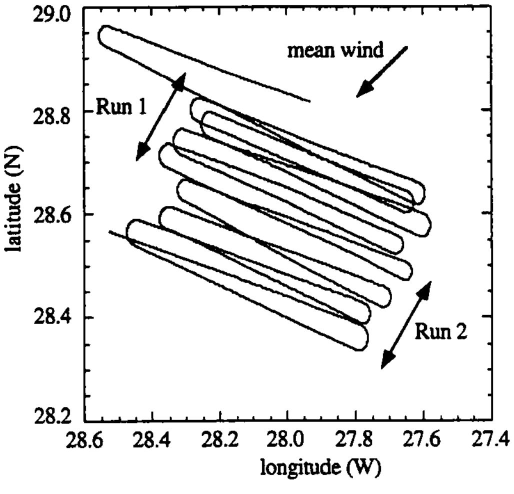

Figure 3. Position of the aircraft during flight A210. The figure shows that the horizontal runs are made so that they are advected along with the mean north-easterly wind.

Flight A210 was the fifth flight of the first 'Lagrangian' experiment. Stratocumulus was encountered during each of the previous four flights of the 'Lagrangian' experiment. Over the five flights the surface layer changed from a slightly stable layer (on RF05) to a slightly convective one (A209, RF06 and RF07). On Run 1 of flight A210 cumulus clouds penetrating into broken stratocumulus above were encountered. Run 2 was flown close to the edge of the cloudy area; during this run the air was typically cloud free (Roode 1994).

In this paper we concentrate on the results of Run 1. This flight consisted of eight horizontal runs (R1.1 to R1.6, R1.8 and R1.9) in, below and above cloud and one porpoise run (R1.7) through the cloud top. The runs were flown so that they were made in roughly

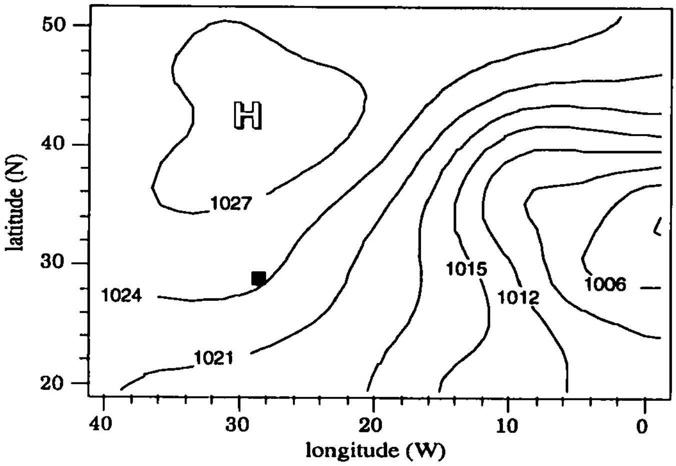

Figure 4. The sea surface pressure in hPa at 1200 UTC 14 June 1992 from the initialized analysis of the ECMWF model. The shaded rectangle indicates the observational area which is the same area as in Fig. 3.

the same airmass, which was advected by the mean wind. Furthermore, the runs were nearly normal to the mean wind direction (Fig. 3).

(*d*) *General weather conditions*

For a review of the synoptic situation during the period of the experiment we used the initialized analysis of the ECMWF (European Centre for Medium-Range Weather Forecasts) model output at 1200 UTC on 14 June 1992. In the observational area a north-easterly wind was induced by a high-pressure zone near position 40 °N, 30 °W, and a low over the continent of Africa at about position 30 °N, 0 °E (Fig. 4). This north-easterly wind caused the observed airmass to be advected equatorwards over sea with gradually increasing sea surface temperatures (SST).

We used the pressure changes as a function of time from every level from the initialized analysis of the ECMWF model to calculate the averaged values over the area 27–30 °W and 27–30 °N. The vertical velocity, ω, in vertical pressure coordinates ($\omega \equiv \mathrm{d}p/\mathrm{d}t$) reduces with the hydrostatic equation approximately to (Holton 1992)

$$\omega \equiv \frac{\mathrm{d}p}{\mathrm{d}t} \cong -\rho g w \tag{1}$$

where p is the pressure, t the time (seconds), ρ the density, g the acceleration due to gravity and w the vertical velocity. Table 2 shows that there is subsidence in the boundary layer and the free atmosphere. An estimation of the divergence from the subsidence (Table 2) gives $-\partial w/\partial z \approx 2 \times 10^{-6}\ \mathrm{s}^{-1}$. To calculate such a small divergence from the continuity equation one needs very accurate wind velocity data. Brümmer (1978) showed that, assuming that the distance between two grid points was of order 100 km, an error of about 1 m s^{-1} in the wind velocity will give an error in the divergence of about $10^{-5}\ \mathrm{s}^{-1}$, which in our case is much larger than the divergence itself. Therefore, radiosonde data from ASTEX were used as an extra tool to estimate the divergence (Nitta and Esbensen 1974). We used measurements from the islands of Porto Santo and Santa Maria and the ships *Valdivia*, *Le Suroit*, *Malcolm Baldridge* and *Oceanus*. All these stations were situated near or at the corners of the ASTEX triangle (Fig. 1), covering an area of about 1000 × 1000 km^2. The calculated divergence averaged over the lowest 1600 m for this area at 1200 UTC 14 June

TABLE 2. THE AREA-AVERAGED SUBSIDENCE VELOCITY AT DIFFERENT HEIGHTS ESTIMATED FROM THE INITIALIZED ECMWF ANALYSIS AT 1200 UTC ON 14 JUNE 1992. THE AVERAGING IS APPLIED OVER THE AREA 27–30 °W AND 27–30 °N.

Height (m)	Subsidence velocity ($\mathrm{cm\,s^{-1}}$)
150	0.02
350	0.13
650	0.23
950	0.20
1350	0.16
1800	0.19
2250	0.43

1992 was found to be small and slightly negative ($-\partial w/\partial z \approx -1 \times 10^{-6}$). This value, and the one derived from the ECMWF model seem to indicate that the divergence is negligibly small.

3. RESULTS

(a) *Mean state of the boundary layer*

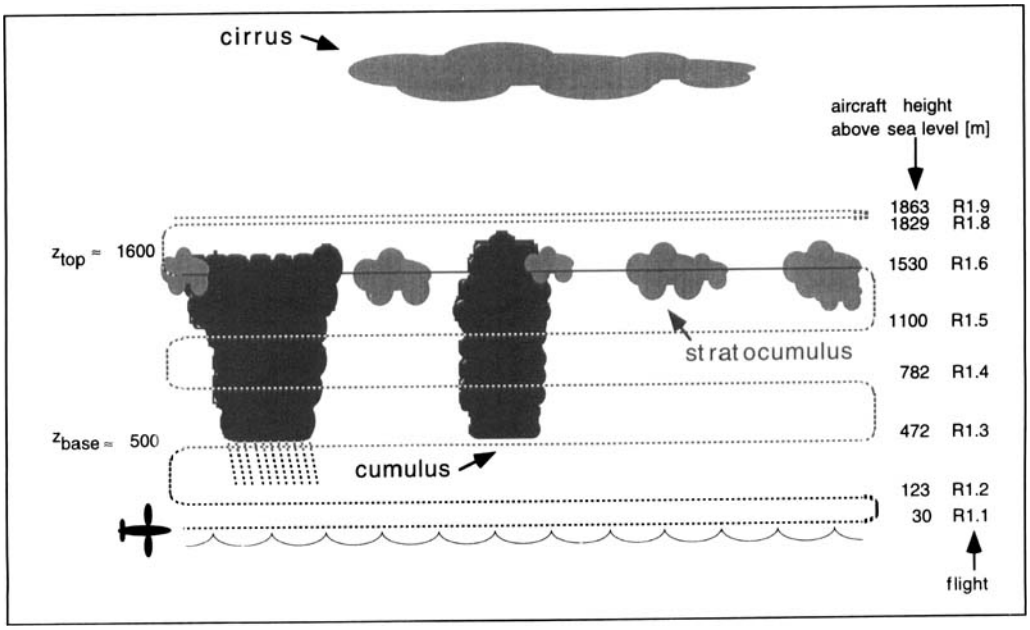

Figure 5. Schematic picture of the clouds observed during Run 1: cumulus and stratocumulus in the boundary layer and high cirrus clouds in the free troposphere.

(i) *Clouds and water content.* A schematic description of the cloud situation is shown in Fig. 5. Analysis of the time series of the liquid-water content of the horizontal runs revealed isolated segments of clouds occurring on runs R1.4 and R1.5, with maximum

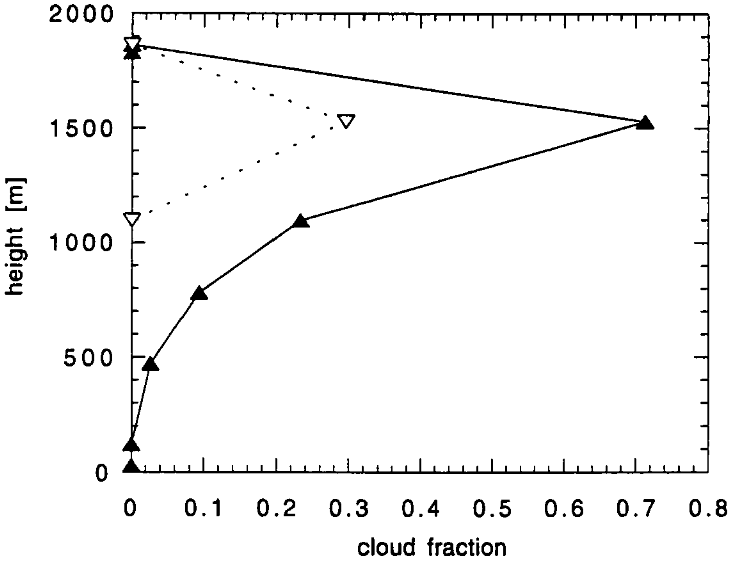

Figure 6. The total cloud fraction (black triangles) as a function of height during Run 1. The open triangles represent the estimated stratocumulus fraction.

values of q_l reaching, typically, around 0.3 and 0.4 g kg^{-1}, respectively. These clouds were found mainly in the western half of the runs. Similar patterns occurred on run R1.6 and the porpoise run R1.7, where peak values of the liquid-water content were as high as 1.0 g kg^{-1}. However, on run R1.6 the clouds were no longer solely isolated. Segments of clouds on the entire horizontal stretch were observed having values of q_l significantly lower than 0.15 g kg^{-1}. From pilot observations these clouds were classified as thin and broken stratocumulus patches, whereas clouds with their cloud base situated at about 500 m were classified as cumulus clouds. On run R1.7 clouds were seen to spread out under the inversion layer and even to penetrate into the inversion. Cloud tops reached altitudes varying between 1590 m and 1660 m. On run R1.3 we found an isolated area where q_l reached a maximum value of about 0.15 g kg^{-1}. According to pilot observations this was due mainly to precipitation from cumulus clouds, which evaporated before reaching the surface.

We calculated the cloud fraction as being that fraction in which the FSSP derived liquid-water content was greater than 0.001 g kg^{-1}. As shown in Fig. 6, the cloud fraction increased from cloud base to a maximum of 72% near cloud top. From Fig. 7(a) it is obvious that, on average, the boundary-layer air is not totally saturated, indicating that the cloud deck is broken; this latter fact is also clear from the liquid-water profile of P1 (Fig. 7(b)). The maximum horizontal mean liquid-water content was found near cloud top (R1.6) where q_l was about 0.09 g kg^{-1}. The inversion was observed to be inhomogeneous. We estimated the average inversion layer height to be approximately 1600 m. Table 3 summarizes the values of the jumps of several parameters across the inversion.

(ii) *Temperature and wind.* In Figs. 8(a) and (b) the virtual potential, and equivalent potential, temperature profile during P1 are shown together with the mean values from the horizontal runs. The virtual potential temperature at the surface is calculated with the assumption that at the sea-surface interface the air is saturated and that the temperature equals the MRF modified barometric radiometer observed SST, approximately 21.1 ± 0.1 °C. From Fig. 8(a) it is clear that the surface layer is unstable because of the local

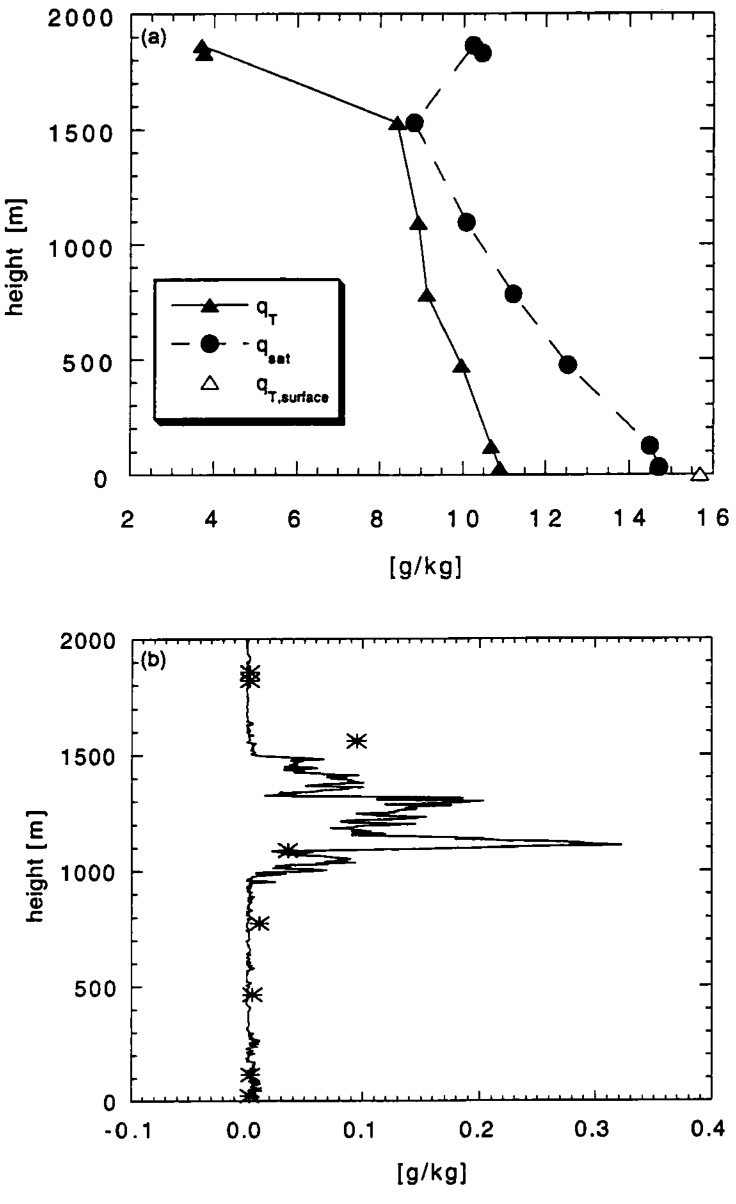

Figure 7. (a) The total water content together with the saturation values as a function of height. The surface value (open triangle) is calculated assuming saturation at sea surface temperature. Here, the dots and triangles represent horizontal mean values. (b) The mean liquid water content (stars) for Run 1 measured by the J–W meter. The solid line was obtained during Profile 1 in which broken stratocumulus was present between 1000 and 1500 m.

maximum of θ_v. The limit of free convection for dry processes is at about 1100 m, which is much lower than the observed cloud tops. The θ_v-profile (from P1) shows a well-mixed layer from 30 m up to about 1000 m. Nevertheless, a slight increase in θ_v can be found at approximately 500 m; an increase of this amount was more obvious in other profile flights and is associated with decoupling. Above 1000 m the gradient is positive (approximately wet adiabatic) owing to the presence of stratocumulus clouds. However, horizontal mean

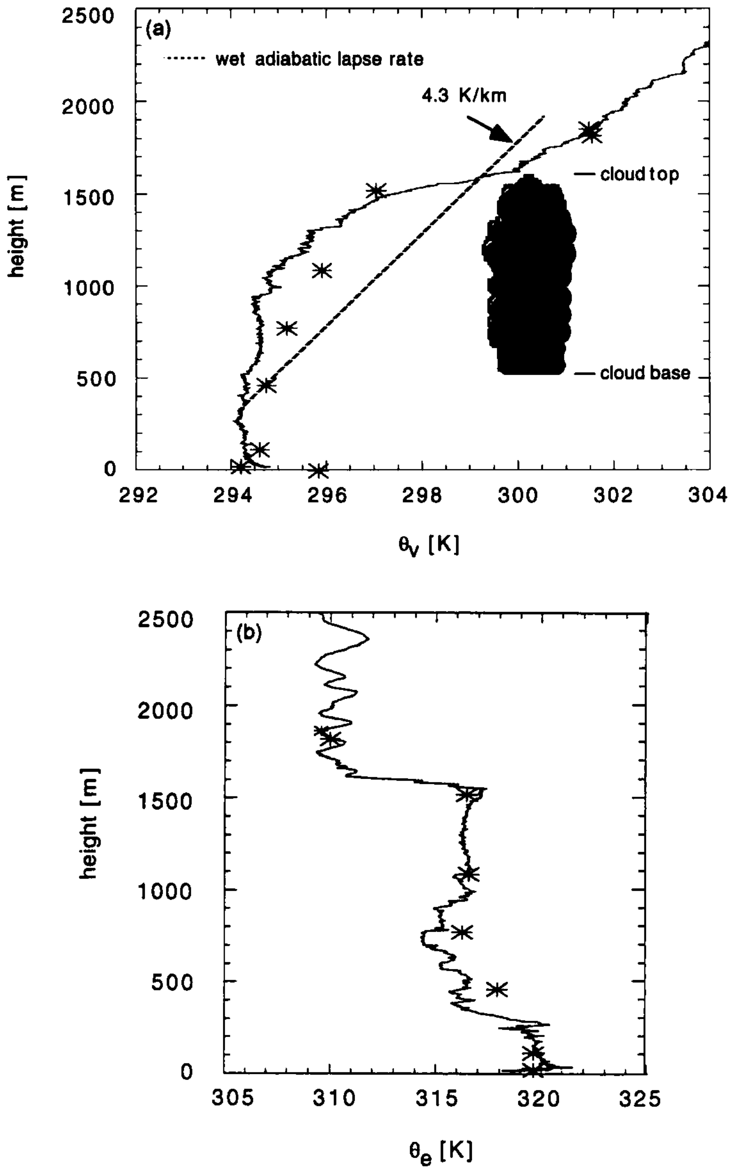

Figure 8. (a) The virtual potential temperature, θ_v. (b) Equivalent potential temperature, θ_e. (c) Eastward velocity, u. (d) Northward velocity, v, as a function of height. Symbols and continuous line as in Fig. 7(b).

values on Run 1 show an increase in θ_v from 500 m upwards with a gradient of 2.1 K km^{-1}. Since the saturated adiabatic lapse rate is about 4.3 K km^{-1}, this layer is conditionally unstable.

The equivalent potential temperature (Fig. 8(b)) is lower in the cloud layer than in the subcloud layer. Investigation of the same airmass two days earlier (Duynkerke *et al.* 1995) showed a solid stratocumulus deck with precipitation. On flight RF07 a decoupling of the cloud layer from the subcloud layer was observed near cloud base (approx. 600 m) (Duynkerke 1995). This decoupling led to a dissipation of stratocumulus, the remnants of which were still visible on flight A210. After the decoupling, θ_e in the subcloud layer increased on account of the increase in surface temperature, whereas θ_e above 500 m

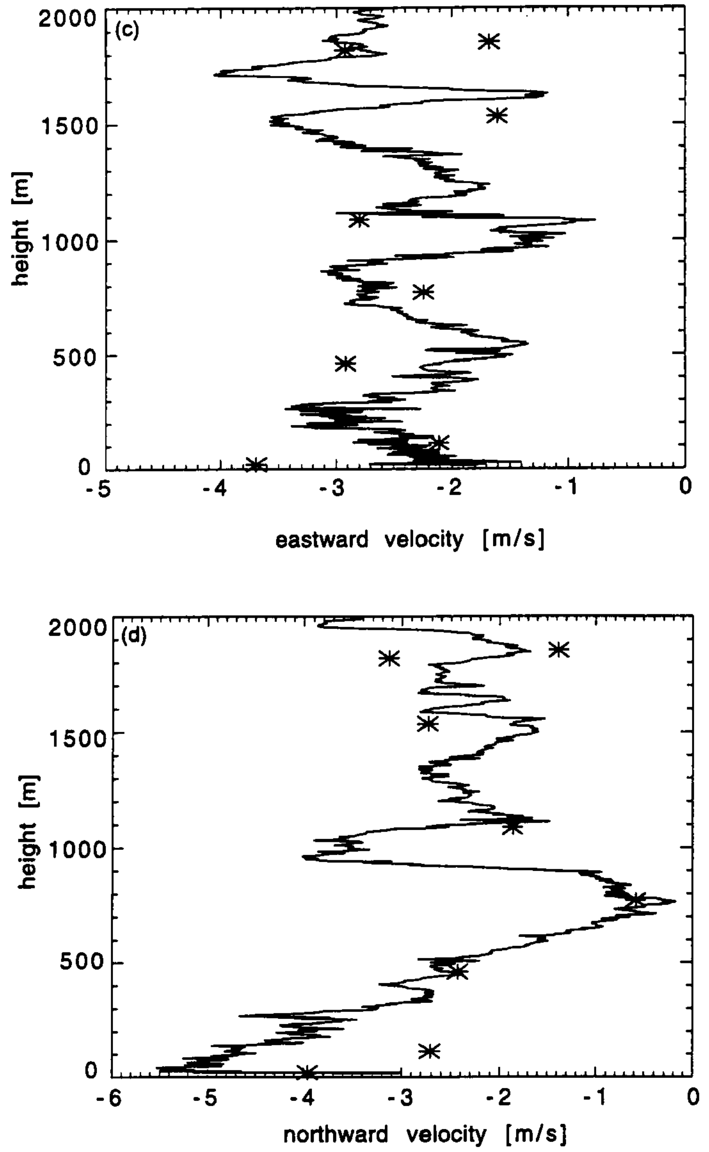

Figure 8. Continued.

hardly increased at all. So a possible explanation for the state of the boundary layer during flight A210 was decoupling of the subcloud layer from the cloud layer causing a breakup of stratocumulus followed by convection in the subcloud layer and subsequent formation of cumulus clouds on top of surface induced thermals.

Lilly (1968) suggested that cloud-top entrainment instability (CTEI) could occur when air from the free atmosphere, entrained into the top of a stratocumulus cloud, was cold and dry enough ($\Delta\theta_e < 0$) to cause sufficient evaporative cooling, so that the mixed parcel would sink and generate TKE. Randall (1980) and Deardorff (1980) suggested that

TABLE 3. A SUMMARY OF THE OBSERVED BOUNDARY-LAYER PROPERTIES DURING RUN 1.

Inversion height	(m)	1600
Cloud base (z_b)	(m)	500
Cloud top (z_t)	(m)	1600
$\Delta\theta_v$	(K)	4.45
$\Delta\theta_e$	(K)	-6.60
Δq_v	(g kg^{-1})	-4.72
Δq_l	(g kg^{-1})	-0.09
Δq_T	(g kg^{-1})	-4.81

The difference, Δ, is taken as the difference between the free troposphere value (R1.8 and R1.9) and the highest boundary-layer value (R1.6), which, to a good approximation, represents the jump across the inversion.

entrainment would occur if

$$\Delta\theta_e < K \left(\frac{L_v}{c_p}\right) \Delta q_T \tag{2}$$

where the constant K is about 0.23, L_v is the latent heat of condensation, c_p is the specific heat of dry air at constant pressure and $\Delta\theta_e$ and Δq_T are the jumps of the equivalent potential temperature and the total water content across the inversion, respectively. MacVean and Mason (1990) discussed this criterion and suggested that K should be larger, namely about 0.7, which would make the criterion more restrictive. From our calculations, where we used the latter value for K and the results given in Table 3, it follows that the observed cloud top does not fulfil the condition (2), and thus should be stable. On the other hand, with $K = 0.23$ (Randall 1980; Deardorff 1980) we find that the cloud layer is unstable.

As a tracer for mixing of air between the boundary layer and the free atmosphere the ozone content can be used. Although the absolute value of the measured ozone was not correct, a significantly higher average ozone content was found on the horizontal runs in the free atmosphere compared with the boundary layer. Porpoise-run observations through the cloud top showed increased ozone contents, relative to the boundary layer, in some cloud segments, suggesting that mixing with free atmospheric air had occurred. A possible explanation for this mixing could be that because of the relatively high upward vertical velocities in cloud, which were observed to be of order 1–2 m s^{-1} in run R1.6 (not shown), the cumuli could penetrate the inversion.

Throughout the boundary layer and free atmosphere wind velocities were northeasterly, rather light and about 4 m s^{-1} (Fig. 8(c) and (d)).

(iii) *Radiation.* The horizontal mean values of the longwave radiative fluxes are shown in Fig. 9, together with the profile observations of P1. The downward longwave flux profile in Fig. 9(a) has jumps at about 200, 600 and 850 m, probably because the profile path passes under stratocumulus patches. The horizontal mean values bear a strong resemblance to irradiance profiles observed by Nicholls and Leighton (1986) in stratocumulus. In their observational study on the structure of stratiform cloud sheets they reported a sharp decrease in net longwave flux at the cloud top and a small increase at cloud base. These flux divergences imply radiative cooling at cloud top and a small warming at cloud base. The cooling at cloud top leads to enhanced turbulence as a result of the destabilization of the cloud layer. On run 1 a jump of approximately 40 ± 15 W m^{-2} was found at cloud top

(Fig. 9(b)). To calculate this jump we used the average value from runs R1.8 and R1.9 for the value in the troposphere. Therefore, the presence of the cumuli and the stratocumulus clouds has an important influence on the radiative cooling profile, and this could be a very important mechanism in the cooling of the boundary layer. Since we observed roughly the same pattern as Nicholls and Leighton (1986), one might assume that the amounts of high cirrus cloud do not contribute significantly to the downward longwave irradiance measured above cloud top. In contrast, solar radiation measurements were disturbed by these high clouds, resulting in large horizontal fluctuations in the solar radiation above the boundary layer.

(*b*) *Turbulence structure*

TABLE 4. SCALING PARAMETERS FOR RUN 1.

w^*	(m s^{-1})	0.6
u^*	(m s^{-1})	0.14
L_{MO}	(m)	−30
$T_{\mathrm{v}*}$	(K)	0.007
$q_{\mathrm{T}*}$	(g kg^{-1})	0.03
T_{S}	(°C)	21.1 ± 0.1

For our analysis of the main turbulent characteristics of the boundary layer we use the following scaling parameters (Nicholls 1989):

$$w^* \equiv \left\{2.5(g/T_0)\int_0^h \overline{w'T_{\mathrm{v}}'}\,\mathrm{d}z'\right\}^{1/3} \tag{3}$$

$$T_{\mathrm{v}*} \equiv \frac{w^{*2}T_0}{gh} \tag{4}$$

$$q_{\mathrm{T}*} \equiv \frac{(\overline{w'q_{\mathrm{v}}'} + \overline{w'q_{\mathrm{l}}'})_0}{w^*} \tag{5}$$

Here h represents the inversion height of the boundary layer and the subscript zero denotes the lowest horizontal run. The rather small value of u^* (Table 4) indicates that mechanical shear production does not contribute much to the production of turbulent kinetic energy.

(i) *Variances:*

Velocity. In Fig. 10(a) and (b) the horizontal and vertical velocity variances are shown, respectively. Here the height is scaled as follows:

$$z' = \frac{z - z_{\mathrm{b}}}{z_{\mathrm{t}} - z_{\mathrm{b}}} \tag{6}$$

where z' represents the scaled height, z the actual height, z_{t} the cloud-top height and z_{b} the cloud base (see Table 3). For the vertical velocity variance and the fluxes referred to in this paper we distinguish between in-cloud and clear-air segments. All sampled results are multiplied by their respective area fraction, so that the sum gives the total variance or flux averaged over one run. Furthermore, for the highest in-cloud run, R1.6, we also calculated the stratocumulus and cumulus contribution. From the integral timescale we estimate the relative error in the total vertical velocity variance to be about 10% for subcloud values, 40% for values in the cloud layer, and 50% in the free troposphere (Lenschow *et al.*

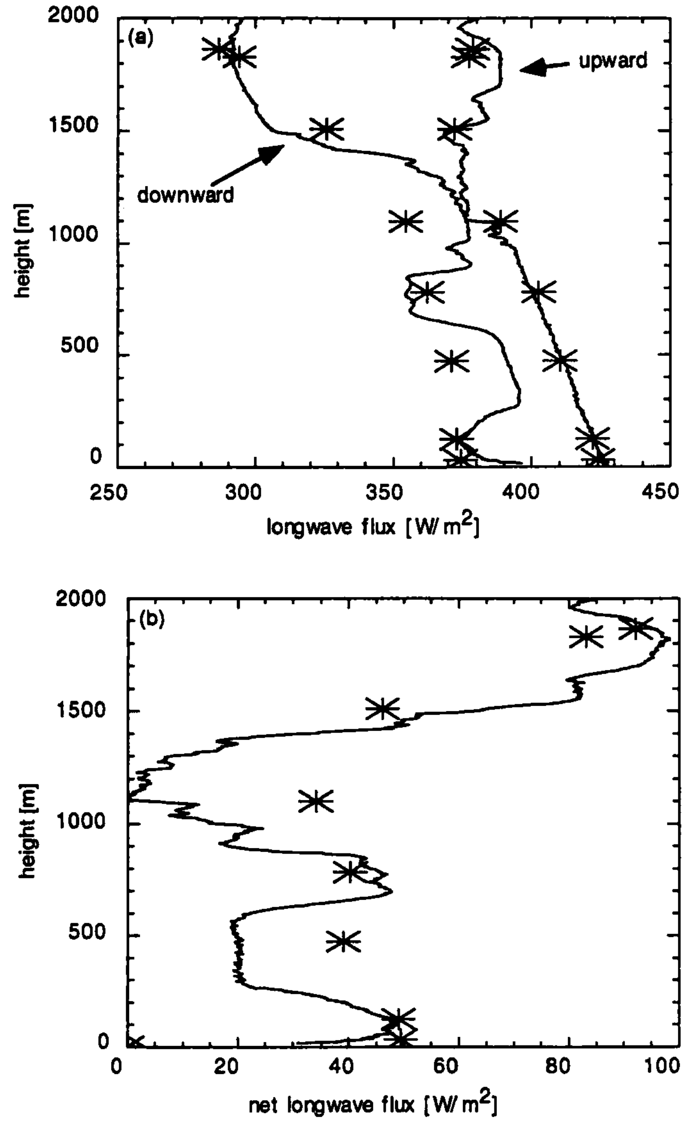

Figure 9. (a) The upward and downward longwave radiation flux. (b) Net longwave radiation as a function of height. Symbols and continuous line as in Fig. 7(b).

1994). The total vertical velocity variance shows an increase from a local minimum at $z' = -0.03$ (R1.3) to a local maximum at $z' = 0.54$ (R1.5). Since the total vertical variance is determined mainly by the cloudy segments this local maximum can be explained in terms of intensifying upward convection caused by the release of latent heat in the clouds. These cloud plumes disturb the mean horizontal flow and result in the strong horizontal-variance increase upwards from the lower cloud layer. At the top of the cloud the vertical updraughts are damped by the stable stratification of the inversion layer, and, since the air motions must satisfy the continuity equation, this must cause the vertical motions to spread out horizontally leaving the updraughts to extend under the inversion layer; which, in turn, explains the peak value in the horizontal variances at $z' = 0.94$ (Nicholls 1989).

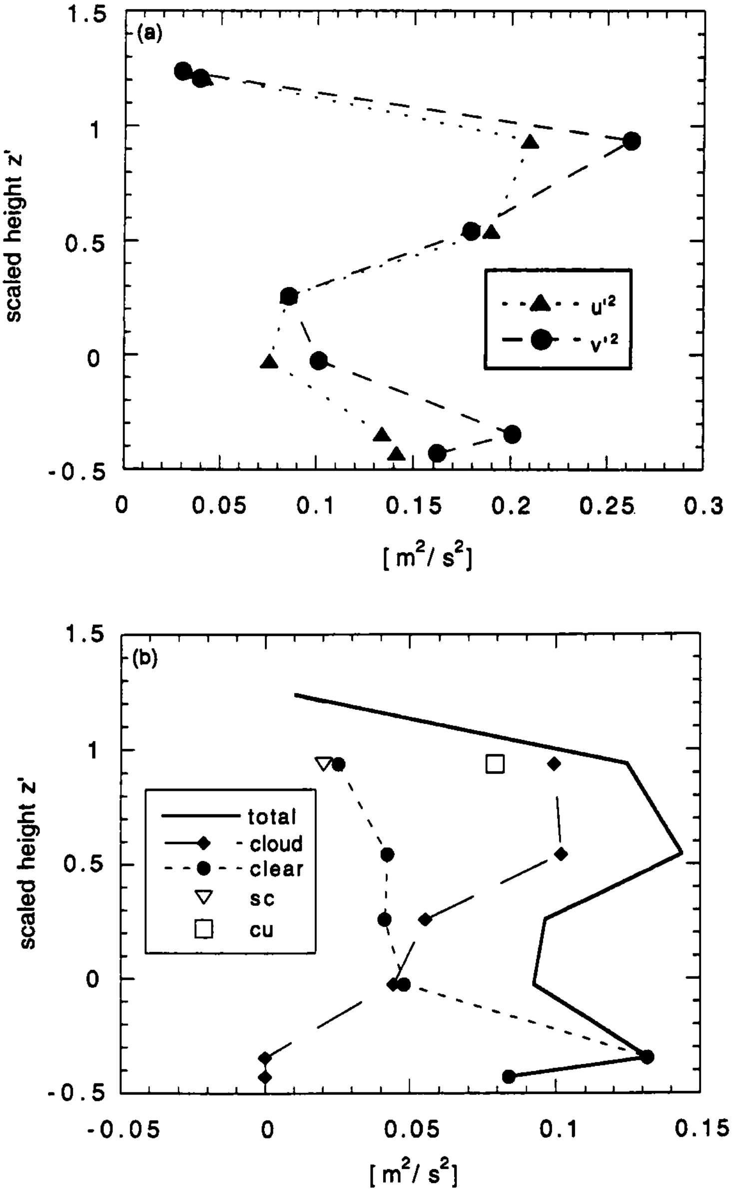

Figure 10. (a) The variance of the horizontal velocities $\overline{u'^2}$ and $\overline{v'^2}$. (b) The vertical velocity $\overline{w'^2}$, as a function of scaled height, z'. The vertical velocity variance has been split up into clear-air and in-cloud parts. For the highest run in cloud also a distinction has been made for cumulus (cu) and stratocumulus (sc), their sum giving the total in-cloud flux. For plot symbols see legend.

A comparison of the total vertical-velocity variances with LES (Large Eddy Simulation)-model results of buoyancy-driven cumulus, obtained by Nicholls *et al.* (1982) and Cuijpers *et al.* (1996), shows fair agreement. These authors simulated cumulus clouds as observed during GATE (Nicholls and LeMone 1980) and found a maximum vertical variance in the middle of the subcloud layer and in the middle of the cloud layer: the latter value was about half the subcloud-layer value. The vertical velocity variances that they found in the upper cloud were quite low, in contrast with the Run-1 observations. A

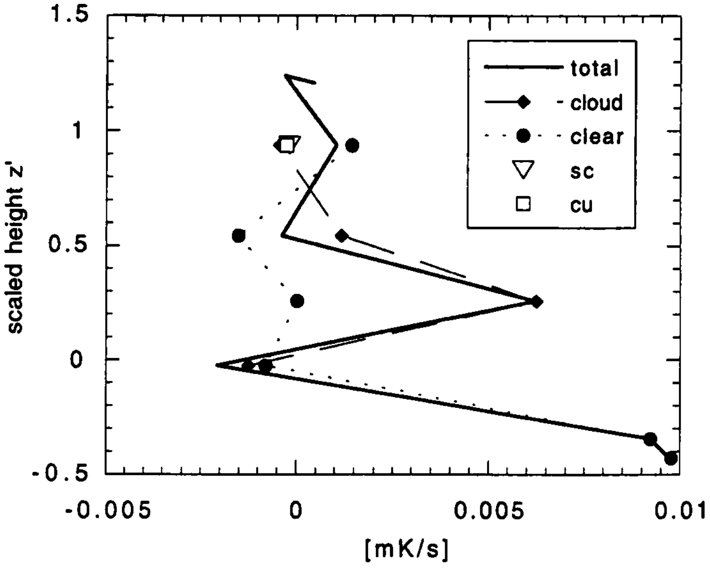

Figure 11. The total, in-cloud and clear-air virtual potential temperature flux, $\overline{w'\theta_v'}$, as a function of scaled height, z'. For the highest run in cloud also a distinction is made for cumulus (cu) and stratocumulus (sc), their sum giving the total in-cloud flux. For plot symbols see legend.

possible explanation is that in the GATE observations there was no strong inversion, the cumuli were small and the cloud cover low. So probably the vertical velocity of the cumuli just gradually weakened with height, whereas on Run 1 clouds were penetrating into the stable inversion. The reason that these clouds could rise steeply and reach the inversion layer might be that there was more conditional unstable stratification in the cloud layer ($d\theta_v/\,dz \approx 2\,\mathrm{K\,km^{-1}}$) compared with GATE ($d\theta_v/\,dz \approx 3.5\,\mathrm{K\,km^{-1}}$). Furthermore, since the cumulus-cloud fraction near the cloud top is relatively high, the longwave radiative loss could give rise to the formation of cold downdraughts, which also would contribute to the vertical velocity variance.

The decrease in the variance of the wind components which occurs towards the surface is due partly to the damping of large-scale eddies, which means that relatively more energy is contained in the small-scale eddies, which cannot be measured. With a cut-off wavelength, λ_c, of 6 m the contribution of the unresolved scales to the vertical velocity variance was about 10% during run R1.1.

(ii) *Fluxes.* Lenschow *et al.* (1994) showed that the systematic error in the flux is given by $2F\mathcal{L}_{ws}L^{-1}$, where F is a vertical flux, $\mathcal{L}_{ws}$ an Eulerian length scale, and L the filter length. We found a maximum integral length scale in the middle of the boundary layer: $\mathcal{L}_{ws} = 550$ m. This means that the error in the flux in the middle of the boundary layer can be estimated to be about 40%, while at the other levels the error will vary between 10 and 30%.

Virtual potential temperature flux. Temperature fluxes were calculated using the measurements of the Rosemount thermometer. We assumed that wetting was not causing serious errors in the measurements since there was no evidence of cold spikes when the aircraft left the cloud during horizontal runs. The total virtual potential-temperature flux (Fig. 11) decreases with height from the surface upwards, reaching a negative value near cloud base. Thus, near the cloud base, rising thermals will be cooler than the environment. This may be due to a rise in virtual potential temperature in the conditionally unstable

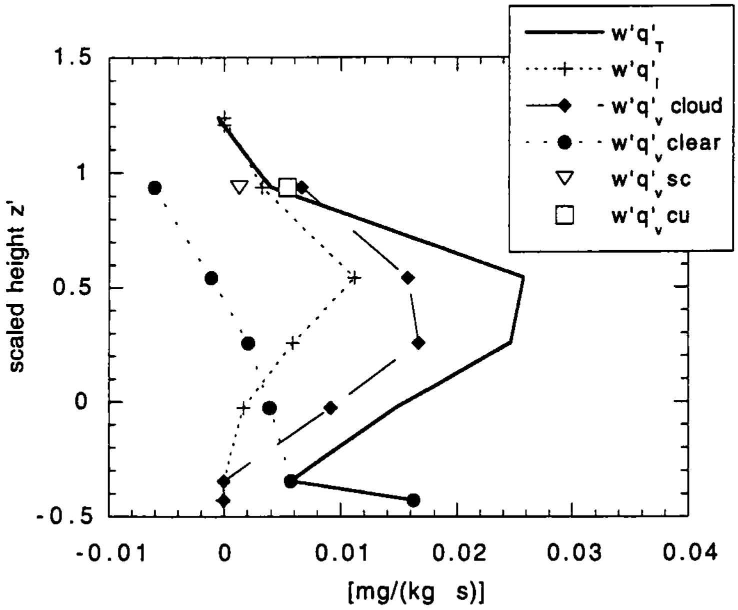

Figure 12. The in-cloud (sc= stratocumulus; cu=cumulus) and clear-air vertical flux of water vapour, $\overline{w'q'_v}$, liquid water, $\overline{w'q'_l}$, and total water, $\overline{w'q'_T}$, as a function of scaled height, z'. For plot symbols see legend.

layer. In spite of the negative buoyancy of the rising thermals, their inertia may cause these thermals to reach the lifting condensation level (LCL). At this stage droplets will form by condensation thus releasing latent heat. Above the LCL the total buoyancy flux is determined mainly by the in-cloud flux. The cloud parcel follows the wet adiabatic, reaching the level of free convection and acquiring a positive buoyancy again. A maximum in buoyancy flux is found at $z' = 0.25$. The rather low amounts of cloud flux above $z' = 0.54$ are surprising. This means that in the upper half of the cloud layer the buoyancy flux in the cloud is almost in a state of neutral buoyancy. The measurements of the vertical velocity in cumulus clouds at this height show fluctuations of about 1–2 m s^{-1} around the mean value. An upward velocity of this order of magnitude is probably sufficient to enable the cumuli to rise several hundreds of metres through the conditionally unstable layer up to the inversion layer.

Liquid water, vapour and drizzle flux. The horizontally averaged drizzle flux was found to be negligibly small. The gravitational settling of droplets was only 10% of the total water flux near cloud top where the total water flux was relatively small. From Fig. 12 and from the equation for total water,

$$\frac{\partial \overline{q_T}}{\partial t} = -\frac{\partial \overline{w'q'_T}}{\partial z}, \tag{7}$$

we found that total water is being transported from the lower levels to higher levels in the boundary layer, thus the upper cloud layer was becoming more humid. The liquid-water flux also contributes to a net wetting of the upper cloud layer. The result is that the total water is redistributed from the lower 1100 m ($z' = 0.54$) upwards to the layer between 1100 and 1600 ($z' \approx 1$).

Equivalent potential-temperature flux. The profile of the vertical equivalent potential-temperature flux, $\overline{w'\theta'_e}$, can indicate whether radiation plays an important part at the top of

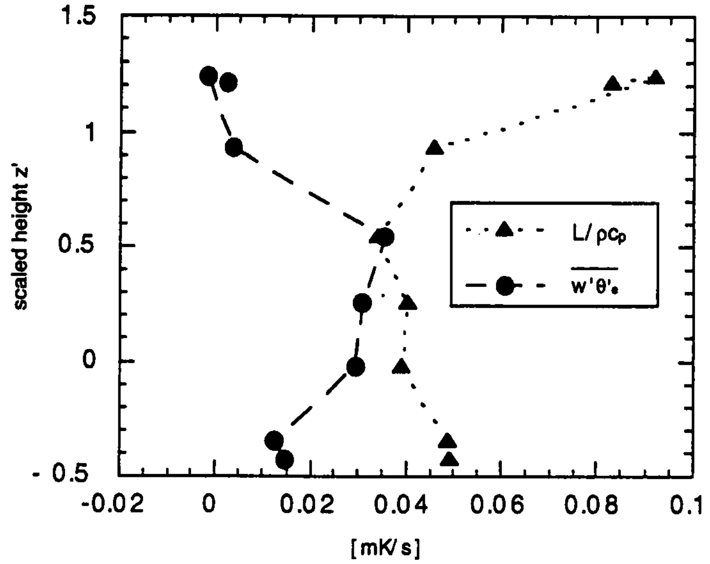

Figure 13. The equivalent potential temperature flux, $\overline{w'\theta_e'}$, and net longwave radiation, L, as a function of scaled height, z'. For plot symbols see legend.

the cloud. Let us consider the hypothetical situation in which there is no, or only a little, subsidence, no precipitation and no horizontal advection. Then it can be shown that the following relationship holds (Deardorff 1976):

$$\frac{\partial \theta_e}{\partial t} + \frac{\partial}{\partial z}\overline{w'\theta_e'} = -\frac{1}{\rho c_p}\frac{\partial S}{\partial z} - \frac{1}{\rho c_p}\frac{\partial L}{\partial z}, \tag{8}$$

where S stands for the net shortwave radiation flux, and L for the net longwave radiation flux. Equation (8) shows that, in a stationary situation, divergence in the radiance will lead to a change in the equivalent potential-temperature flux of opposite sign.

Figure 13 shows that the radiative cooling at cloud top is compensated for partly by heating, because of the equivalent potential-temperature flux. The difference between the radiative cooling and the heating due to the equivalent potential-temperature flux can probably be attributed to absorption of solar radiation.

Observations show that during daytime, and in solid cloud conditions, absorption of solar radiation in the cloud can lead to decoupling, provided the heat flux at the surface is small (Nicholls and Leighton 1986; Turton and Nicholls 1987). The turbulence in the cloud layer will then become decoupled from turbulence in the subcloud layer, leaving a stable transition layer between the cloud and subcloud layer. Decoupling is assumed to be an important mechanism in the stratocumulus–cumulus transition process (Rogers *et al.* 1995). In this case solar absorption probably will not dominate the longwave radiative loss. The latter acts mainly near the top of the cloud, where the cloud fraction is maximum. On the other hand, solar absorption is a process which occurs deeper in the cloud layer, and will diminish from cloud top towards cloud base as a result of the decreasing cloud fraction.

Mass flux. Many cumulus convection schemes are based on the assumption that the vertical mass transport within cloud can be described in terms of cumulus updraughts and

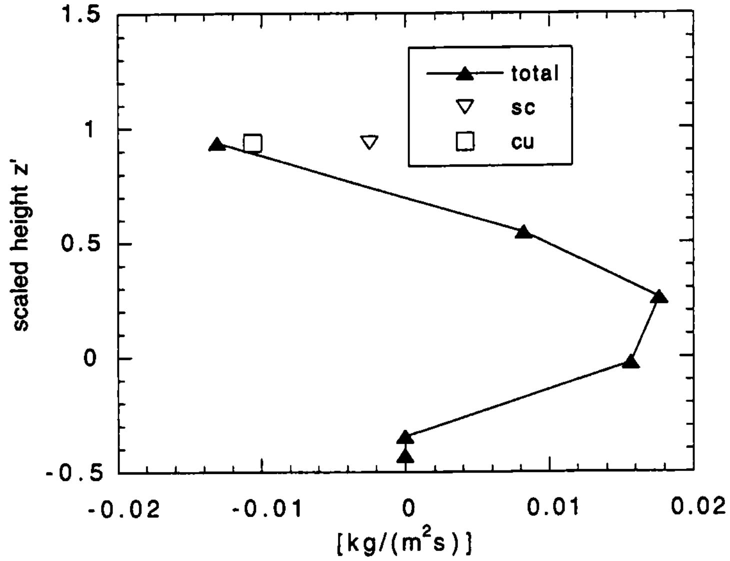

Figure 14. The vertical mass flux in cloud as a function of scaled height, z'.

compensating environmental subsidence. In this way, any variation of the mass flux with height is a measure of entrainment/detrainment of air. For example, an increasing mass transport with height can be interpreted as clear environmental air being mixed into the cloudy air through lateral entrainment. A difficulty encountered in parametrizing the mass flux is that it is dependent on the stage of development of the cumulus cloud. Grinnell *et al.* (1996) showed that in the earliest stage of cumulus development the mass flux through the bulk of the cloud layer was upwards, while at the mature and later stages a negative mass flux prevailed, mainly as a result of precipitation-driven downdraughts.

We calculated the in-cloud mass flux as $M = \rho w_u a_u$, with ρ the density (kg m^{-3}), w_u the average vertical velocity in cloud, and a_u the cloud fraction. A maximum mass flux was found in the lower half of the cloud (Fig. 14), above which it decreased to a negative value near the top of the cloud. This indicates that the cumulus clouds are in the mature or later stage (Grinnell *et al.* 1996). As a possible explanation for this downward mass flux these authors suggested that the cumuli penetrate into the inversion, mix with the dry inversion air so that cloud droplets evaporate, after which the cooled air descends. Furthermore, longwave radiative loss at the top of the cloud will produce cold downdraughts. The mass flux just below cloud base is the result of a strong updraught in a shower.

(iii) *Third-order moments:*

Turbulent kinetic energy flux. In Fig. 15(a) the turbulent kinetic energy flux is shown. The errors in the third-order moment, $\overline{w'^3}$, are varying between 15% for the lowest run and 90% in the middle of the boundary layer. The positive value of the flux of TKE ($\overline{w'e'}$) in the bulk of the boundary layer indicates that this transport is upwards. Again, in the cloud layer, this flux is determined mainly by the in-cloud flux. Near cloud top a small negative flux is found for the in-cloud flux, which suggests that TKE is transported downwards. Local maxima for TKE transport are found in the subcloud layer and in the middle of the cloud layer.

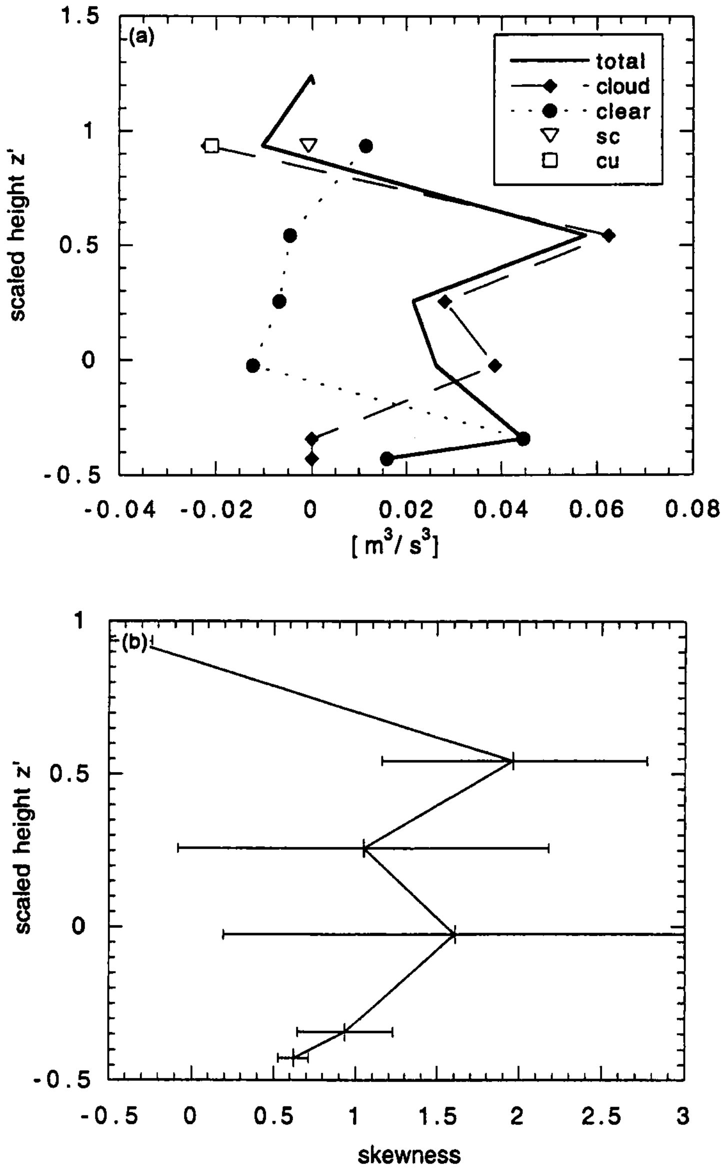

Figure 15. (a) The vertical turbulent kinetic energy flux, $\overline{w'e'}$, as a function of scaled height, z'. For the highest run in cloud also a distinction has been made between cumulus (cu) and stratocumulus (sc), their sum giving the total in-cloud flux. (b) The skewness factor S as a function of scaled height, z'.

Skewness. The skewness parameter, S, is a measure of the distribution of vertical-velocity fluctuations and is defined as

$$S = \frac{\overline{w'^3}}{(\overline{w'^2})^{3/2}}. \tag{9}$$

When S is positive this means that upward motions are the greater and occupy a smaller fractional area than the downward motions, and vice versa. The skewness calculated for Run 1 is shown in Fig. 15(b). The effects of downdraughts can be clearly seen here, since the negative value near the top of the cloud suggests that downdraughts are more intense than the inversion-penetrating updraughts. A maximum value of about 2 for the skewness, S, is found in the middle of the cloud layer, where the vertical velocity variance was also at its maximum. It is remarkable that these maxima do not coincide with the maximum buoyancy flux; this is probably due to the fact that the skewness has its maximum where the acceleration is zero. Nevertheless, both the maximum vertical velocity variance and the skewness confirm the notion that cloud velocities at $z' = 0.54$ are quite high.

4. TURBULENT KINETIC ENERGY BUDGET

(*a*) *Spectral properties*

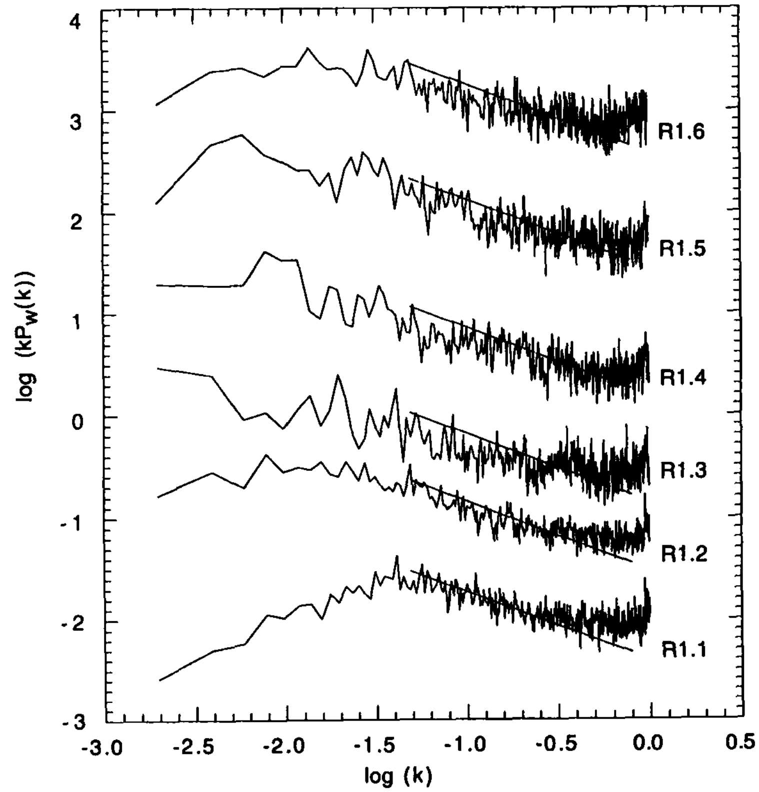

Figure 16. Vertical velocity spectra as a function of wavenumber, k, for the horizontal runs R1.1 to R1.6. The spectra have been shifted vertically by one decade. The straight line is the fit to the spectra in the inertial subrange.

The fast Fourier transform technique was applied to the vertical velocity data for each level of Run 1. To filter out length scales larger than 3 km the time series were split up into intervals of 32 seconds. These reduced data-sets were detrended by subtracting the straight best-fit line from the data segment. The intervals overlapped, so about 30 spectra were obtained for any one level. The spectra presented in this paper are the average of these 30 spectra. By this means the statistical noise was significantly reduced, especially for large wavenumbers, k. In principle, the viscous dissipation, ε, can be calculated from these averaged spectra through the formula

$$P_w = \alpha_w \varepsilon^{2/3} k^{-5/3}, \tag{10}$$

with $\alpha_w = \frac{4}{3} \times 0.5$; k the wavenumber; P_w the spectral intensity. However, for a horizontally inhomogeneous boundary layer a complication arises since ε may vary significantly in each segment. In that case the leg-averaged value of $\overline{\varepsilon^{2/3}}$ is not equal to $\bar{\varepsilon}^{2/3}$, with $\bar{\varepsilon}$ the average dissipation of all individual segments. Since we are interested in ε and not in its 2/3 power we used the latter method to find the dissipation rate. For this purpose the spectral energy was integrated over the wavenumber interval $0.05 \leqslant k \leqslant 0.8\ \mathrm{m}^{-1}$, whereafter the dissipation was found from the expression

$$\varepsilon = \left(\frac{\int_{k_1}^{k_2} P_w \, dk}{\alpha_w \left(-\frac{3}{2}\right) \left(k_2^{-2/3} - k_1^{-2/3}\right)} \right)^{3/2} . \tag{11}$$

The main advantage of integration is that the dissipation is now directly related to the spectral energy which is conserved in this way. This is not the case when $\log P_w$ and $\log k$ are used for a linear fit.

Figure 16 depicts the average spectra of the vertical velocities of runs R1.1 to R1.6. The continuous line shows the $-2/3$ power relation between k and $kP_w(k)$. Variation of the wavenumber interval leads to changes of about 30% in the calculated dissipation rate. The sensitivity of ε to the particular wavenumber interval used is negligible in the high wavenumber range where the spectral energy is low, and vice versa. The opposite is true for a linear fit, where in a logarithmic graph the larger wavenumbers are more densely distributed than are the low wavenumbers and therefore give a relatively higher contribution to the linear fit. The spectrum above the boundary layer (R1.8 and R1.9, not shown here) did not show an inertial subrange because, above the inversion, the air is not turbulent. Near the surface the spectral peak is observed at wavenumbers larger than at the higher levels, which suggests that TKE is contained in relatively small-scale eddies. The results of the dissipation (segment averaged) within the boundary layer are given in Table 5. The maximum dissipation is found near the surface and cloud top. The in-cloud cumulus dissipation rates are of the order $0.001\ \mathrm{m}^2\ \mathrm{s}^{-3}$.

TABLE 5. THE LAYER-AVERAGED AND AVERAGE IN-CLOUD DISSIPATION RATE FOR RUNS R1.1 TO R1.6.

Run	Height (m)	Layer-averaged dissipation ($\mathrm{m}^2\ \mathrm{s}^{-3}$)	In-cloud dissipation ($\mathrm{m}^2\ \mathrm{s}^{-3}$)
R1.1	30	0.0005	
R1.2	123	0.0004	
R1.3	472	0.0001	
R1.4	782	0.0001	0.001
R1.5	1100	0.0003	0.001
R1.6	1530	0.0005	0.0001 (sc) 0.0007 (cu)

The interval used for the best fit was $0.05 \leqslant k \leqslant 0.8\ \mathrm{m}^{-1}$.

(b) *Turbulent kinetic energy budget*

With the turbulent kinetic energy defined as

$$\bar{e} = \frac{1}{2}(\overline{u'^2} + \overline{v'^2} + \overline{w'^2})$$

the TKE budget can be written in the form

$$\frac{d\bar{e}}{dt} = \overset{\mathrm{B}}{\frac{g}{T_0}(\overline{w'\theta'_v})} - \overset{\mathrm{S}}{\left(\overline{u'w'}\frac{\partial \bar{U}}{\partial z} + \overline{v'w'}\frac{\partial \bar{V}}{\partial z}\right)} - \overset{\mathrm{T}}{\frac{\partial(\overline{w'e'})}{\partial z}} - \overset{\mathrm{P}}{\frac{1}{\rho_0}\frac{\partial(\overline{w'p'})}{\partial z}} - \overset{\mathrm{D}}{\varepsilon} \tag{12}$$

where

B = Buoyancy production
S = Shear production
T = Turbulence transport
P = Pressure transport
D = Dissipation of TKE.

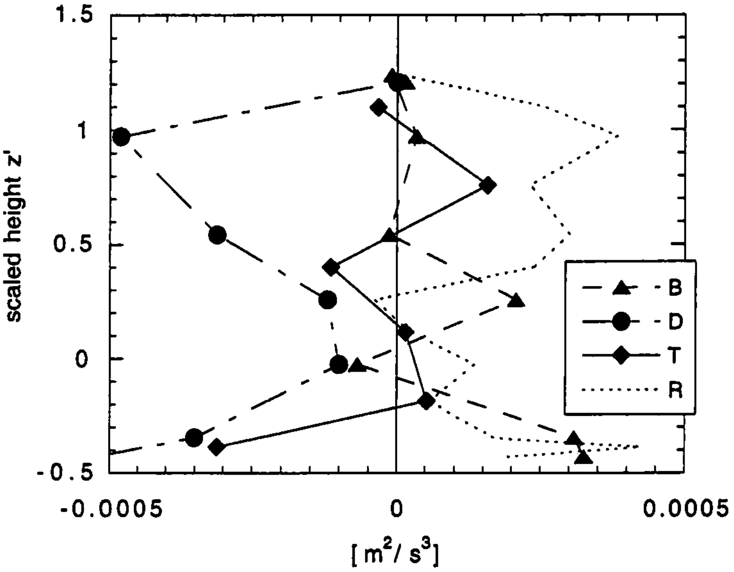

Figure 17. The turbulent kinetic energy budget as a function of scaled height, z': B buoyancy production; D dissipation; S shear production; T turbulent transport; R the residual term.

The pressure transport term, P, is extremely difficult to measure. In a steady-state situation, when $d\bar{e}/dt$ is assumed to be negligibly small, P is often taken to be equal to the sum of B, S, T and D. We calculate the residual, R, as follows:

$$R = -\left\{\frac{g}{T_0}(\overline{w'\theta'_v}) - \frac{\partial(\overline{w'e'})}{\partial z} - \varepsilon\right\}. \tag{13}$$

The TKE budget is shown in Fig. 17. We neglected the wind shear because it was found to be very small. For run R1.1 the ratio z/L is approximately unity and B and S are of about equal importance; for run R1.2 the ratio z/L is approximately 4, and the shear is negligibly small. From Fig. 17 we can see that above 1100 m a gain of TKE comes from the turbulent transport term T, whereas the buoyancy production becomes nearly zero above 1100 m. The latent heat release which supplies the energy for cumulus convection is clearly important since it seems that it is redistributed by the turbulent transport term from the lower cloud layer upwards.

The maximum dissipation rate at the surface and at the top of the cloud is due to the smallness of the turbulence scales close to boundaries, which leads to larger gradients and dissipation rates. Simulations by Cuijpers *et al.* (1996) showed that the pressure transport term was not negligibly small and was therefore important for the TKE budget. Rapid pressure fluctuations are difficult to measure accurately, and were not measured during ASTEX; therefore we do not know the precise role of the pressure transport term. Nevertheless, one would expect that in this kind of convection there would be a significant correlation between pressure and (vertical) velocity perturbations.

5. DISCUSSION AND CONCLUSIONS

This paper discusses the results of an observational study of the mean turbulence and radiative properties of a convective boundary layer in which cumulus clouds penetrated into a thin and broken stratocumulus layer above. For this purpose we used measurements from the UK MRF C-130 aircraft during the first 'Lagrangian' experiment in ASTEX. Upwards from the sea surface the boundary layer can be divided into a mixed layer, a conditionally unstable layer and an inversion layer. The equivalent potential temperature was found to be lower in the cloud layer than in the subcloud layer because of a decoupling (Duynkerke 1995) during an earlier period of the first 'Lagrangian' experiment. According to the stability criterion of MacVean and Mason (1990) the cloud top was stable to cloud-top entrainment. However, from porpoise-run observations through the cloud top we found, in some cloud segments, increased amounts of ozone compared to the amounts in the boundary layer, suggesting that mixing with free atmospheric air had occurred. Observation of the vertical velocities shows that, in our case, entrainment probably could be triggered by the relatively high upward vertical velocity within the cumulus clouds.

Turbulent kinetic energy was generated by the advection of boundary-layer air over a gradually increasing sea surface temperature and by longwave radiative cooling at the top of the clouds. The maximum values for TKE were found near the surface and near the top of the boundary layer. The dissipation rate was also found to be at its maximum near the bottom and near the top of the boundary layer.

A study of the fluxes showed that the buoyancy flux decreased from a maximum near the surface to a slightly negative value near the base of the cumuli. Because of the release of latent heat and the resulting upward velocities the cumuli were able to reach the level of free convection (Stull 1985). In the cloud layer the buoyancy flux was determined mainly by the in-cloud flux. Above the level of free convection the buoyancy flux was positive towards the middle of the cloud layer. From the middle of the cloud layer upwards the buoyancy decreased rapidly.

The buoyancy flux in the subcloud layer was found to be similar to that measured during GATE (Nicholls and LeMone 1980) and to the simulations done subsequently by Nicholls *et al.* (1982) and Cuijpers *et al.* (1996). The main difference between the simulations of Cuijpers *et al.* and our measurements is to be found in the cloud layer. The model results showed that the buoyancy flux decreased gradually from the middle of the cloud layer upwards, becoming nearly zero near the top of the cloud. However, we found that the buoyancy flux was already very small by the middle of the cloud layer.

The energy supply needed for overshooting was found to come from the vertical turbulent-transport term. This term was responsible for a redistribution of TKE from the lower part of the cloud layer towards the upper part, and because of the vertical fluxes of liquid water and vapour, the upper part of the cloud layer was being moistened. In this way water was redistributed, so counteracting the dissipation of the stratocumulus deck.

In the bulk of the boundary layer, turbulent convection was dominated by intensive narrow updraughts, as can be seen from the skewness parameter, S. Up to the middle of the cloud layer the skewness was found to be positive and rather large. Values ranged from about 1 ± 0.3 above the surface layer to a maximum of about 2 ± 0.8 in the middle of the cloud layer. This shows that the upward velocity was quite high and was obviously sufficient for the clouds to reach the inversion, despite the lack of positive buoyancy in the middle of the cloud layer.

At the top of the cloud turbulence was driven by cloud-top cooling caused by longwave radiative loss. This loss was found to be about $-(40 \pm 15)$ W m^{-2} and, as a result, the cloud layer was destabilized. A small negative skewness and rather high vertical velocity variance near the cloud top suggests that downward convection is slightly more intense than upward convection. This is also found from the vertical mass-flux profile, which shows an upward mass flux decreasing with height to a negative value near the top of the cloud. This downward convection can be due to a cooling of air due to the formation of radiatively cooled downdraughts or to mixing and evaporation of liquid water in the unsaturated air of the inversion. Furthermore, spreading of the cumuli under the inversion layer led to a divergence of air, which resulted in compensating downward motions.

6. ACKNOWLEDGEMENT

The investigations were supported in part by the Netherlands Geosciences Foundation (GOA) with financial aid (grant 750.295.03A) from the Netherlands Organization for Scientific Research (NWO). The aircraft data were kindly provided by Dr Doug Johnson of the UK Meteorological Research Flight. Radiosonde data were organized and supplied by Bill Syrett of The Pennsylvania State University. We are very grateful to Piet Jonker who provided the computer programs, and to Bert Holtslag and Hans Cuijpers for carefully reading and helping to improve the manuscript.

REFERENCES

Albrecht, B. A., Penc, R. S. and Schubert, W. H.	1985	An observational study of cloud-topped mixed layers. *J. Atmos. Sci.*, **42,** 800–822
ASTEX	1992	Operations plan, prepared by the Fire Project Office and ASTEX Working Group, March 1992. This document is available from: NASA Langley Research Centre, Mail Stop 438, Hampton, VA 23665-5225
Augstein, E., Riehl, H., Ostapoff, F. and Wagner, V.	1973	Mass and energy transports in an undisturbed Atlantic trade wind flow. *Mon. Weather Rev.*, **101,** 101–111
Bretherton, C. S. and Pincus, R.	1995	Cloudiness and marine boundary-layer dynamics in the ASTEX Lagrangian experiments. Part I: Synoptic setting and vertical structure. *J. Atmos. Sci.*, **52,** 2707–2723
Bretherton, C. S., Austin, P. and Siems, S. T.	1995	Cloudiness and marine boundary-layer dynamics in the ASTEX Lagrangian experiments. Part II: Cloudiness, drizzle, surface fluxes and entrainment. *J. Atmos. Sci.*, **52,** 2724–2735
Brost, R. A., Lenschow, D. H. and Wyngaard, J. C.	1982a	Marine stratocumulus layers. Part I: Mean conditions. *J. Atmos. Sci.*, **39,** 800–817
Brost, R. A., Wyngaard, J. C. and Lenschow, D. H.	1982b	Marine stratocumulus layers. Part II: Turbulence budgets. *J. Atmos. Sci.*, **39,** 818–836
Brümmer, B.	1978	Mass and energy budgets of a 1 km high atmospheric box over the GATE C-scale triangle during undisturbed and disturbed weather conditions. *J. Atmos. Sci.*, **35,** 997–1011
Caughey, S. J. and Kitchen, M.	1984	Simultaneous measurements of the turbulent and microphysical structure of nocturnal stratocumulus cloud. *Q. J. R. Meteorol. Soc.*, **110,** 13–34
Caughey, S. J., Crease, B. A. and Roach, W. T.	1982	A field study of nocturnal stratocumulus. II: Turbulence structure and entrainment. *Q. J. R. Meteorol. Soc.*, **108,** 125–144

Cuijpers, J. W. M., Duynkerke, P. G. and Nieuwstadt, F. T. M. 1996 Analyses of variance and flux budgets in cumulus-topped boundary layers. *Atmos. Res.*, **40,** 307–337

Deardorff, J. W. 1976 On the entrainment rate of a stratocumulus-topped mixed layer. *Q. J. R. Meteorol. Soc.*, **102,** 563–582

1980 Cloud top entrainment instability. *J. Atmos. Sci.*, **37,** 131–147

Driedonks, A. G. M. and Duynkerke, P. G. 1989 Current problems in the stratocumulus-topped atmospheric boundary layer. *Boundary-Layer Meteorol.*, **46,** 275–304

Duynkerke, P. G. 1995 Cloud dynamics and microphysics during the first 'Lagrangian' of the ASTEX experiment. Pp. 240–243 in *Proc. 11th Symp. on boundary layers and turbulence*. American Meteorology Society

Duynkerke, P. G., Zhang, H. Q. and Jonker, P. J. 1995 Microphysical and turbulent structure of nocturnal stratocumulus as observed during ASTEX. *J. Atmos. Sci.*, **52,** 2763–2777

Gerber, H., Arends, B. G. and Ackerman, A. S. 1994 New microphysics sensor for aircraft use. *Atmos. Res.*, **31,** 235–252

Grinnell, S. A., Bretherton, C. S., Stevens, D. E. and Fraser, A. M. 1996 Vertical mass flux calculations in Hawaiian trade cumulus clouds from dual-Doppler radar. *J. Atmos. Sci.* (in press)

Hignett, P. 1991 Observations of diurnal variation in a cloud-capped marine boundary layer. *J. Atmos. Sci.*, **48,** 1474–1482

Holland, J. Z. and Rasmusson, E. 1973 Measurements of the atmospheric mass energy and momentum budgets over a 500 kilometre square of tropical ocean. *Mon. Weather Rev.*, **101,** 44–55

Holton, J. R. 1992 *An introduction to dynamic meteorology*, 3rd ed. Academic Press, Inc.

Klein, S. A. and Hartmann, D. L. 1993 The seasonal cycle of low stratiform clouds. *J. Clim.*, **6,** 1587–1606

LeMone, M. and Pennell, W. T. 1976 The relationship of trade wind cumulus distribution to subcloud layer fluxes and structure. *Mon. Weather Rev.*, **104,** 524–539

Lenschow, D. H., Mann, J. and Kristensen, L. 1994 How long is long enough when measuring fluxes and other turbulence statistics? *J. Atmos. Oceanic Technol.*, **11,** 661–673

Lilly, D. K. 1968 Models of cloud-topped mixed layers under a strong inversion. *Q. J. R. Meteorol. Soc.*, **94,** 292–309

MacVean, M. K. and Mason, P. J. 1990 Cloud top entrainment instability through small-scale mixing and its parameterization in numerical models. *J. Atmos. Sci.*, **47,** 1012–1030

Nicholls, S. 1984 The dynamics of stratocumulus: Aircraft observations and comparisons with a mixed-layer model. *Q. J. R. Meteorol. Soc.*, **110,** 783–820

1989 The structure of radiatively driven convection in stratocumulus. *Q. J. R. Meteorol. Soc.*, **115,** 487–511

Nicholls, S. and Leighton, J. 1986 An observational study of the structure of stratiform cloud sheets. Part I: Structure. *Q. J. R. Meteorol. Soc.*, **112,** 431–460

Nicholls, S. and LeMone, M. A. 1980 The fair-weather boundary layer in GATE: The relationship of subcloud fluxes and structure to the distribution and enhancement of cumulus clouds. *J. Atmos. Sci.*, **37,** 2051–2067

Nicholls, S., LeMone, M. A. and Sommeria, G. 1982 The simulation of a fair-weather marine boundary layer during GATE using a three-dimensional model. *Q. J. R. Meteorol. Soc.*, **108,** 167–190

Nitta, T. and Esbensen, S. 1974 Diurnal variations in the western Atlantic trades during the BOMEX. *J. Meteorol. Soc. Jpn*, **52,** 254–257

Paluch, I. R. and Lenschow, D. H. 1991 Stratiform cloud formation in the marine boundary layer. *J. Atmos. Sci.*, **48,** 2141–2158

Pennell, W. T. and LeMone, M. A. 1974 An experimental study of turbulence structure in the fair-weather trade wind boundary layer. *J. Atmos. Sci.*, **31,** 1308–1323

Randall, D. A. 1980 Conditional instability of the first kind, upside down. *J. Atmos. Sci.*, **37,** 125–130

Roach, W. T., Brown, R., Caughey, S. J., Crease, B. A. and Slingo, A. 1982 A field study of nocturnal stratocumulus. I: Mean structure and budgets. *Q. J. R. Meteorol. Soc.*, **108,** 103–123

Rogers, D. P. and Telford, J. W. 1986 Metastable stratus tops. *Q. J. R. Meteorol. Soc.*, **112,** 481–500

Rogers, D. P., Yang, X., Norrio, P. M., Johnson, D. W., Martin, G. M., Friehe, C. A. and Berger, B. W. 1995 Diurnal evolution of the cloud-topped marine boundary layer. Part I: Nocturnal stratocumulus development. *J. Atmos. Sci.*, **52,** 2953–2966.

Roode de, S. R. 1994 'Observation of the turbulence structure of trade-wind cumulus clouds'. Master thesis. Institute of Marine and Atmospheric Research, Utrecht, The Netherlands

Slingo, A., Brown, R. and Wrench, C. L. 1982a A field study of nocturnal stratocumulus. III: High resolution radiative and microphysical observations. *Q. J. R. Meteorol. Soc.*, **108**, 145–165

Slingo, A., Nicholls, S. and Schmetz, J. 1982b Aircraft observastions of marine stratocumulus during JASIN. *Q. J. R. Meteorol. Soc.*, **108**, 833–856

Smith, S. A. and Jonas, P. R. 1995 Observations of the turbulent fluxes in fields of cumulus clouds. *Q. J. R. Meteorol. Soc.*, **121**, 1185–1208

Stull, R. B. 1985 A fair-weather cumulus cloud classification scheme for mixed-layer studies. *J. Clim. Appl. Meteorol.*, **24**, 49–56

Stull, R. B. and Elorante, E. W. 1984 Boundary-Layer Experiment—1983. *Bull. Am. Meteorol. Soc.*, **65**, 450–456

Turton, J. D. and Nicholls, S. 1987 Diurnal variation of stratocumulus. *Q. J. R. Meteorol. Soc.*, **113**, 969–1009

Weaver, C. J. and Pearson Jr., R. 1990 Entrainment instability and vertical motion as causes of stratocumulus breakup. *Q. J. R. Meteorol. Soc.*, **116**, 1359–1388